Fluid Flow and Entropy Generation Analysis of Al$_2$O$_3$–Water Nanofluid in Microchannel Plate Fin Heat Sinks

Hao Ma [ID]**, Zhipeng Duan *, Liangbin Su, Xiaoru Ning, Jiao Bai and Xianghui Lv**

School of Mechanical, Electronic and Control Engineering, Beijing Jiaotong University, Beijing 100044, China
* Correspondence: zpduan@bjtu.edu.cn; Tel.: +86-10-5168-8542; Fax: +86-10-5168-8404

Abstract: The flow in channels of microdevices is usually in the developing regime. Three-dimensional laminar flow characteristics of a nanofluid in microchannel plate fin heat sinks are investigated numerically in this paper. Deionized water and Al$_2$O$_3$–water nanofluid are employed as the cooling fluid in our work. The effects of the Reynolds number ($100 < Re < 1000$), channel aspect ratio ($0 < \varepsilon < 1$), and nanoparticle volume fraction ($0.5\% < \Phi < 5\%$) on pressure drop and entropy generation in microchannel plate fin heat sinks are examined in detail. Herein, the general expression of the entropy generation rate considering entrance effects is developed. The results revealed that the frictional entropy generation and pressure drop increase as nanoparticle volume fraction and Reynolds number increase, while decrease as the channel aspect ratio increases. When the nanoparticle volume fraction increases from 0 to 3% at $Re = 500$, the pressure drop of microchannel plate fin heat sinks with $\varepsilon = 0.5$ increases by 9%. It is demonstrated that the effect of the entrance region is crucial for evaluating the performance of microchannel plate fin heat sinks. The study may shed some light on the design and optimization of microchannel heat sinks.

Keywords: pressure drop; entropy generation; nanofluids; microchannels; heat sinks; entrance effects; electronic cooling

---

1. Introduction

Recent advances in manufacturing technologies have driven the development of microelectronicmechanical systems (MEMS) [1]. The greatest challenge is overheating due to an increasing power flux and a higher thermal resistance in electronic chips [2]. Significant heat dissipation generated by the electronic chips requires a special cooling system [3]. One of the most potential applications for MEMS is the microchannel heat sink, and it has been successfully utilized for controlling the temperature in various microdevices [4].

Accurate modeling of fluid flow and heat transfer is quite important for numerous MEMS applications [5]. The recent development of microscale fluid systems has attracted much academic research of fluid flow and heat transfer in microchannels with different cross-sections [6–14].

Morini et al. [7] examined the effect of the viscous dissipation on the friction factor and convective heat transfer in microchannels. Liu and Garimella [8] investigated, both experimentally and numerically, liquid flow in microchannels. Onset of turbulence was verified by flow visualization in their work. Wang [10,11] investigated analytically forced convection heat transfer in rectangular ducts with various aspect ratios. Vocale et al. [12] numerically investigated the gas flow through elliptical microchannels with slip flow boundary conditions. Si Salah et al. [13] numerically studied the flow in two-dimensional rectangular microchannels using the control volume finite element method without pressure correction.

Several investigations on the developing flow in microchannels have been carried out [15–22]. Wen and Ding [16] pointed out the remarkable enhancement of convective heat transfer utilizing

nanofluids, particularly in the entrance region. Mishan et al. [17] highlighted the importance of entrance effects in evaluating of the performance micro-scale heat sink. Renksizbulut et al. [20] studied numerically gas flow and heat transfer in the entry region of rectangular microchannels with velocity slip conditions.

In recent years, a great number of studies have been conducted utilizing innovative geometries [23–33], employing liquid coolants with excellent thermal features [34–41], and applying micro-pin-fins [42–44] in order to improve the capabilities of microchannel heat sinks (MCHS) removing the heat generated by electronic chips.

Pang et al. [23] proposed an optimized cooling structure for avionics applications using a multiobjective optimal design method. Vinodhan and Rajan [24] numerically investigated the overall performance of four new microchannel heat sink configurations. Lu and Vafai [25] carried out a comparative study of MCHS with different layers. Wang et al. [26] performed a numerical research on the thermal performance of MCHS with a series of trapezoidal grooves. Soleimanikutanaei et al. [31] carried out a numerical study of the heat transfer enhancement through utilizing transverse microchannels in heat sinks. Al Siyabi et al. [32] conducted an experimental research on the performance of a multilayered microchannel heat sink. Deng et al. [33] numerically examined the behavior of double-layered microchannel heat sinks with different cross-sectional shapes.

Alternative coolants have been required due to high rate of the heat generated by increasingly powerful electronics. Xie et al. [34] presented a numerical analysis on the heat transfer and friction characteristics of a minichannel heat sink using water. Nasiri et al. [37] numerically investigated the entropy generation in MCHS with Fe_3O_4–water. Bahiraei and Heshmatian [38] pointed out that nanofluids containing grapheme and silver nanoparticles result in excellent thermal characteristics. Sarafraz et al. [41] evaluated the thermal performance of MCHS with rectangular microchannel employing silver–water nanofluid. Milanese et al. [45] and Iacobazzi et al. [46] presented important mechanisms of high thermal conductivity of nanofluids. Iacobazzi et al. [47] investigated the effect of clustering phenomenon on thermal conductivity of Al_2O_3-water nanofluid. Duan et al. [48] focused on sphere drag and heat transfer, and their work is of great significance for modeling nanofluid flow. Fan et al. [42] proposed a novel cylindrical oblique fin minichannel heat sink fitted over cylindrical heat sources. Kanargi et al. [43] investigated the behavior of an air-cooled, planar, oblique-finned heat sink for two oblique angles.

Ribs mounted in MCHS generally result in a heat transfer enhancement [49]. Khan et al. [50] conducted a three-dimensional numerical simulation of MCHS with ribbed channels in various configurations. Chai et al. [51] carried out a numerical analysis of the thermal performance of an interrupted microchannel heat sink with ribs in the transverse microchambers.

Efficiency enhancement of thermal systems is a concern for engineers. Entropy generation minimization [52,53] and the principle of least action [54–56] are two important methods to study the performance optimization of a thermal system. Some efforts have been made to research into the entropy generation of different thermal systems [23,37,57–68]. Khan et al. [59] studied the performance of MCHS using an entropy generation minimization procedure, and proposed a general expression evaluating irreversibilities. Awad [60] amply reviewed thermodynamic optimization studies of microchannels based on entropy generation analysis. Some suggestions for future work were put forward by Lorenzini and Mahian [67] in the field of entropy generation in nanofluid flows.

Flow in the channels of MCHS usually cannot reach the fully developed regime. However, researchers and engineers have generally assumed microchannel heat sink flows to be fully developed, ignoring entrance effects. A literature survey demonstrates a detailed analysis of MCHS nanofluids entrance flows has not yet been reported. This paper concentrates on the pressure drop and entropy generation characteristics of microchannel plate fin heat sinks operated with nanofluids considering entrance effects.

The purpose of this study is to investigate the flow and entropy generation characteristics on three-dimensional developing laminar flow of Al_2O_3-water nanofluid in microchannel heat sinks with various aspect ratios of rectangular channels.

In this research, three-dimensional numerical models have been established to evaluate the laminar flow and entropy generation characteristics in microchannel plate fin heat sinks. The effects of the Reynolds number, channel aspect ratio, and volume fraction of Al_2O_3–water nanofluid on pressure drop and entropy generation characteristics in microchannel plate fin heat sinks are analyzed.

2. Mathematical Model

2.1. Physical Model and Assumptions

The physical model of a microchannel plate fin heat sink is shown in Figure 1a. The length of the heat sink is *L*, the width is *W*, and the height is *H*. The top surface is insulated and the bottom surface is uniformly heated. As the coolant passes through the rectangular microchannels along the *z* axis, it removes the heat generated by the electronic component attached below. Due to good thermophysical properties and high economy of Al_2O_3–water nanofluid, most researchers utilized them as research objects [69]. Hence, deionized water and Al_2O_3–water nanofluid were employed as the cooling fluid in our work. There are *N* rectangular channels, and each channel has a height 2*a* and width 2*b*. The thickness of each fin is *t*.
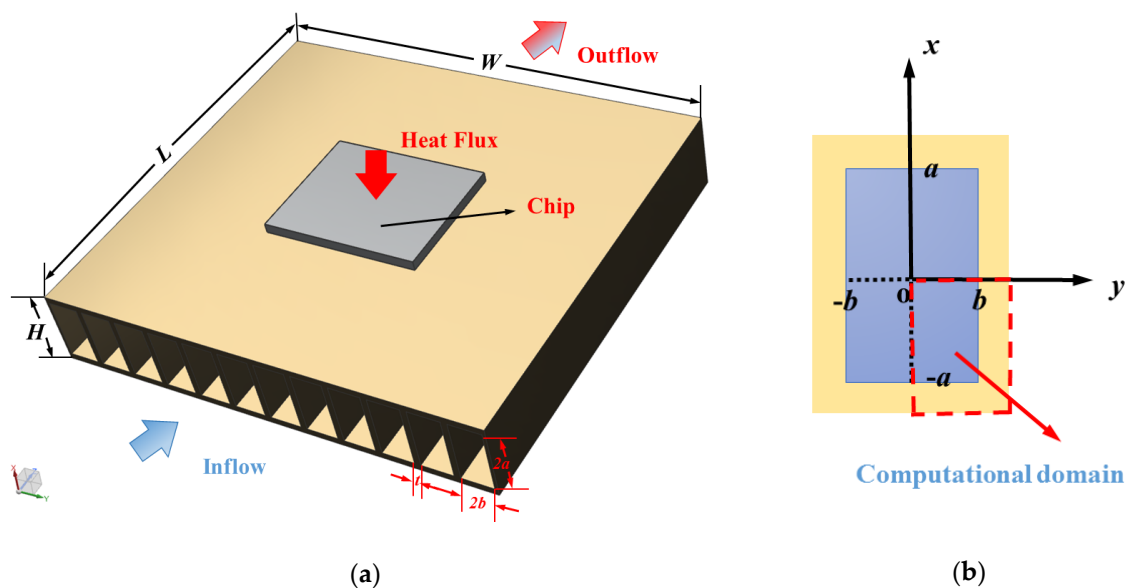
Figure 1. Schematics of the microchannel plate fin heat sink. (**a**) Microchannel plate fin heat sink and (**b**) rectangular channel.

Taking advantage of the symmetry, a quarter of the rectangular channel as shown in Figure 1b is chosen as the numerical model to reduce computation cost. The nanofluid can be treated as incompressible Newtonian fluid and the thermophysical properties are assumed to be constant in this study [70,71]. The dimensions of the computational domain in this work are presented in Table 1.

Table 1. Dimensions of the computational domain in present work.

ε	a (μm)	b (μm)	D_h (μm)	L (mm)	Mesh (Computational Domain)
0.1	1100	110	400	14	$700 \times 165 \times 17$
0.2	600	120	400	14	$700 \times 90 \times 18$
0.3	433	130	400	14	$700 \times 65 \times 20$
0.4	350	140	400	14	$700 \times 53 \times 21$
0.5	300	150	400	14	$700 \times 45 \times 23$
0.6	267	160	400	14	$700 \times 40 \times 24$
0.7	243	170	400	14	$700 \times 37 \times 25$
0.8	225	180	400	14	$700 \times 34 \times 27$
0.9	211	190	400	14	$700 \times 32 \times 28$
1	200	200	400	14	$700 \times 30 \times 30$

The hydraulic diameter of channels D_h is held constant and the length L is 14 mm. The width and height of the channel are varied with aspect ratios. The aspect ratio ε of a rectangular channel is defined as

$$\varepsilon = \frac{b}{a} \tag{1}$$

and the hydraulic diameter of a rectangular channel is defined as

$$D_h = \frac{4A}{P} = \frac{2ab}{a+b} \tag{2}$$

2.2. Governing Equations

The continuum approach is valid in this study [1]; the continuity and momentum equations are solved numerically considering nanoparticle volume fraction. The governing transport equations of mass and momentum are as follows.

Continuity equation:

$$\nabla \cdot \vec{U} = 0 \tag{3}$$

Momentum equation:

$$\rho_{nf}\vec{U}(\nabla \cdot U_i) = -\nabla P + \mu_{nf}\nabla^2 U_i, i = 1, 2, 3 \tag{4}$$

A uniform velocity profile is given at the inlet and no counterflow at the outlet.

2.3. Thermophysical Properties

Single phase flow of Al_2O_3–water nanofluid with four different volume fractions (ϕ = 0.5, 1, 3, and 5 percent) is employed in current work. Based on the properties of deionized water and Al_2O_3 particles tabulated in Table 2, the effective density, specific heat capacity [72], viscosity [73], and thermal conductivity [74] are calculated using the following expressions.

$$\rho_{nf} = (1-\phi)\rho_{bf} + \phi\rho_p \tag{5}$$

$$\left(\rho C_p\right)_{nf} = (1-\phi)\left(\rho C_p\right)_{bf} + \phi\left(\rho C_p\right)_p \tag{6}$$

$$\frac{\mu_{nf}}{\mu_{bf}} = (1-\phi)^{-2.5} \tag{7}$$

$$\frac{k_{nf}}{k_{bf}} = 1 + 64.7\phi^{0.7460}\left(\frac{d_{bf}}{d_p}\right)^{0.3690}\left(\frac{k_p}{k_{bf}}\right)^{0.7460} Pr^{0.9955}Re^{1.2321} \tag{8}$$

where k, μ, ρ, and Cp denote the thermal conductivity, dynamic viscosity, density, and specific heat capacity, respectively. The subscripts *bf*, *p*, and *nf* represent base fluid (deionized water), nanoparticle, and nanofluid, respectively. The simulation parameters of thermophysical properties of Al_2O_3–water nanofluid are presented here in Table 3.

Table 2. Thermophysical properties of base fluid (deionized water) and Al_2O_3 particles.

Material [Reference]	ρ (kg/m^3)	Cp (J/kgK)	k (W/mK)	μ (Pa·s)	d_p (nm)
Deionized water [39]	996	4178	0.611	0.000859	-
Al_2O_3 [70]	3380	765	30	-	47

Table 3. Simulation parameters of thermophysical properties of Al_2O_3–water nanofluid.

Nanofluids	Φ (%)	ρ (kg/m^3)	Cp (J/kgK)	μ (Pa·s)
Al_2O_3-water	0.5	1007.92	4120.77	0.000870
Al_2O_3-water	1	1019.84	4064.88	0.000881
Al_2O_3-water	3	1067.52	3853.81	0.000927
Al_2O_3-water	5	1115.20	3660.79	0.000977

2.4. Fluid Flow Analysis

Applying the method of scale analysis to compare the force scale between friction and inertial forces, the nondimensional channel length ξ can be obtained:

$$\frac{\mu \frac{\partial^2 u}{\partial y^2}}{\rho u \frac{\partial u}{\partial x}} \sim \frac{\mu \frac{U}{D_h^2}}{\frac{\rho U^2}{L}} = \frac{L}{D_h Re_{D_h}} = \xi \tag{9}$$

When $\xi \gg 1$, the fully developed flow momentum equation in rectangular channels is expressed as

$$\frac{\partial^2 u}{\partial x^2} + \frac{\partial^2 u}{\partial y^2} = \frac{1}{\mu}\frac{dp}{dz} \tag{10}$$

The Fanning friction factor f is given by the following equation.

$$f = \frac{\Delta P}{2\rho u_m^2 z / D_h} \tag{11}$$

For fully developed laminar flow in rectangular channels, Shah and London [75] provided the expression of the friction factor Reynolds number product as follows

$$fRe = 24\left(1 - 1.3553\varepsilon + 1.9467\varepsilon^2 - 1.7012\varepsilon^3 + 0.9564\varepsilon^4 - 0.2537\varepsilon^5\right) \tag{12}$$

Further, a more accurate theoretical solution was developed by Duan and Muzychka [76,77], and is expressed as

$$fRe_{D_h} = \frac{24}{(1 + \varepsilon)^2\left[1 - \frac{192\varepsilon}{\pi^5}\left(\tanh\left(\frac{\pi}{2\varepsilon}\right) + \frac{1}{243}\tanh\left(\frac{3\pi}{2\varepsilon}\right)\right)\right]} \tag{13}$$

Flow in the channels of MCHS usually cannot reach the fully developed regime. Considering the developing region, the pressure drop equations are expressed in terms of an apparent friction factor as follows

$$\Delta P = \frac{2\left(f_{app}Re\right)\mu u_m z}{D_h^2} \tag{14}$$

2.5. Entropy Generation Analysis

The analysis of entropy generation to evaluate the behavior of thermal devices is a practical technique. The volumetric entropy generation rate $\dot{S}'''_{gen,t}$ can be presented as [78]

$$\dot{S}'''_{gen,t} = \dot{S}'''_{gen,h} + \dot{S}'''_{gen,f} \tag{15}$$

where $\dot{S}'''_{gen,h}$ and $\dot{S}'''_{gen,f}$ are the 3D volumetric thermal and viscous entropy generation rates, respectively, and are expressed as [78]

$$\dot{S}'''_{gen,h} = \frac{k_{nf}}{T^2}\left(\left(\frac{\partial T}{\partial x}\right)^2 + \left(\frac{\partial T}{\partial y}\right)^2 + \left(\frac{\partial T}{\partial z}\right)^2\right) \tag{16}$$

$$\dot{S}'''_{gen,f} = \frac{\mu_{nf}}{T}\left[2\left(\left(\frac{\partial u}{\partial x}\right)^2 + \left(\frac{\partial v}{\partial y}\right)^2 + \left(\frac{\partial w}{\partial z}\right)^2\right) + \left(\frac{\partial u}{\partial y} + \frac{\partial v}{\partial x}\right)^2 + \left(\frac{\partial u}{\partial z} + \frac{\partial w}{\partial x}\right)^2 + \left(\frac{\partial w}{\partial y} + \frac{\partial v}{\partial z}\right)^2\right] \tag{17}$$

The global entropy generation rates are given by the integration of the volumetric entropy generation rates over the whole domain as follows

$$\dot{S}_{gen,h} = \int \dot{S}'''_{gen,h} dV \tag{18}$$

$$\dot{S}_{gen,f} = \int \dot{S}'''_{gen,f} dV \tag{19}$$

$$\dot{S}_{gen,t} = \int \dot{S}'''_{gen,t} dV \tag{20}$$

The total entropy generation rate can be conveniently calculated by the following expression [59].

$$\dot{S}_{gen,t} = \dot{Q}\left[\frac{1}{T_a} - \frac{1}{T_b}\right] + \frac{\dot{m}\Delta P}{\rho T_a} \tag{21}$$

where T_a, T_b, and $\dot{Q}$ represent the ambient temperature, the temperature of the heat sink base and heat transfer rate, respectively. Substituting Equation (14) into Equation (21), the global entropy generation rate considering entrance effects is obtained as follows

$$\dot{S}_{gen,t} = \dot{Q}\left[\frac{1}{T_a} - \frac{1}{T_a}\right] + \frac{2(f_{app}Re)\dot{m}\mu u_m z}{\rho T_a D_h^2} \tag{22}$$

3. Numerical Method

A computational fluid dynamics software, ANSYS Fluent 18.0, which can be applied to facilitate the investigation of fluid flow characteristics in microchannels [8], was employed to solve the governing equations. Uniform inlet velocity is specified and uniform inlet temperature of the working fluid is set to 290 K. Moreover, zero relative pressure is utilized on the outlet and no slip velocity boundary conditions are applied to the walls. The SIMPLE algorithm was adopted to deal with the coupling between velocity and pressure. Considering the accuracy of calculations, double precision was used and second-order upwind scheme was applied on momentum equations. The convergence criterion for the residuals of the continuity equation and momentum equations were less than 1×10^{-9}.

The whole computational domain was meshed using hexahedral elements and performed in structured grids. The mesh in the streamwise direction had a double successive ratio of 1.013 near the entrance and 1.005 near the outlet. The grid sensitivity test was conducted for more accurate numerical results with less computational cost. The comparison of three different grid density distributions of $500 \times 20 \times 20$, $700 \times 30 \times 30$, and $900 \times 40 \times 40$ were established at the aspect ratio $\varepsilon = 1$ of rectangular

fluid domain. The $f_{app}Re$, at the entrance region, changed by 1.52% from the first to the second mesh, and only varied by less than 0.65% upon further refinement to the finest grid. In view of the calculation accuracy and time cost, the second one was chosen as the grid to get mesh independent solution. The meshes of other aspect ratios had also been tested and the mesh quantities are shown in Table 1.

## 4. Results and Discussion

4.1. Model Validation

Firstly, in order to verify the correctness of the numerical method, the numerical simulations of ten different aspect ratios of rectangular microchannels are implemented. The results of Poiseuille number in the fully developed laminar flow of rectangular channels is obtained by numerical calculation. Figure 2 demonstrates the comparison between the current results and the available numerical data from Shah and London [75] and the available analytical data from Duan and Muzychka [76]. It is found that the difference between the current results and available data from Shah and London [75] is less than 0.2%. The maximum difference between the current results and available data from Duan and Muzychka [76] is less than 0.3%.
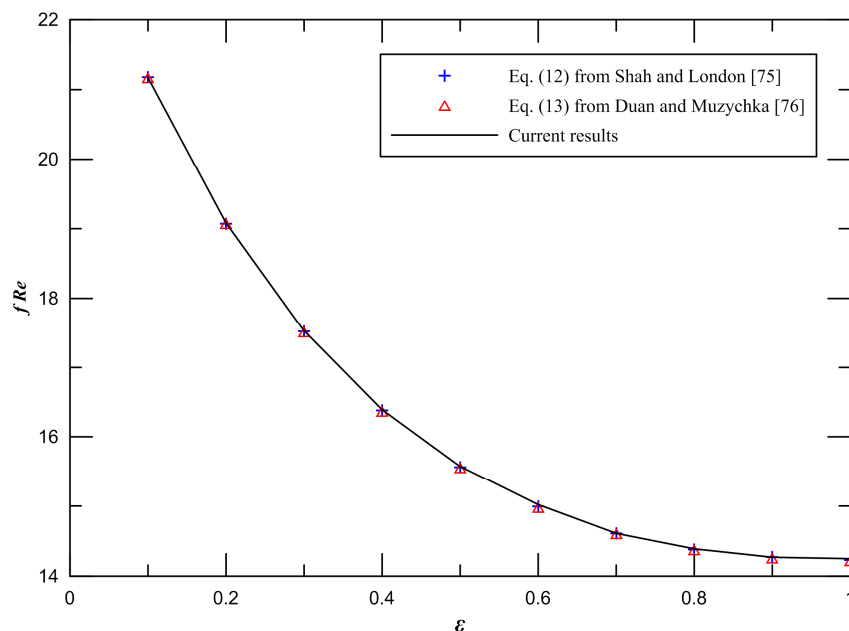
Figure 2. Comparison of *fRe* for Shah and London [75] and Duan and Muzychka [76] at an aspect ratio of 1.

Secondly, we pay attention to friction characteristics of the entry region of rectangular microchannels. It is presented that the comparison between the obtained results of the apparent friction factor and the available results from Shah and London [75] and Duan et al. [79] when the aspect ratio $\varepsilon = 1$ in Figure 3. It is observed that our numerical results agree with the available numerical data [75,79] quite well. The maximum difference between the current results and the available numerical data is less than 5.9%, which does prove the numerical means used is valid.
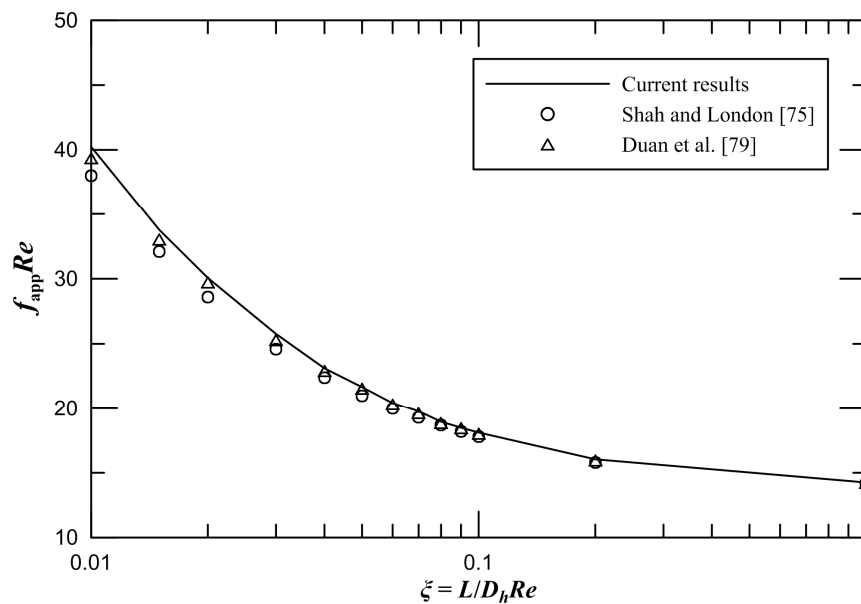
**Figure 3.** Comparison of $f_{app}Re$ for Shah and London [75] and Duan et al. [79] at an aspect ratio of 1.

4.2. Effect of Reynolds Number on Pressure Drop and Frictional Entropy Generation

For the 1 vol.% Al_2O_3–water nanofluid, three-dimensional numerical simulations of rectangular microchannel heat sinks with aspect ratio $\varepsilon = 1$ were carried out in the range of $100 < Re < 1000$. The pressure drop parameter as a function of Reynolds number is shown clearly in Figure 4a. It is seen that the pressure drop monotonically increases along the flow direction in the microchannel heat sink, and the pressure drop observably increases as Reynolds number increases for the same aspect ratio. When the Reynolds number increases from 500 to 1000, the pressure drop of the channel increases by 144%. An increase in the flow velocity of the working fluid leads to a remarkable increase in the flow resistance, thus resulting in a significant pressure drop. Furthermore, it is obviously observed that the higher pressure gradient occurs where L is just less than 4 mm, which corresponding to nondimensional flow distance ranges from 0.01 to 0.1 for different Reynolds numbers, and the pressure drop increases proportionately later along the flow direction in channels for the same Reynolds number.

The effect of Reynolds number on $f_{app}Re$ values of laminar flow in microchannel plate fin heat sinks has been studied first in this work. The variations of $f_{app}Re$ in different Reynolds numbers with the nondimensional flow distance are illustrated in Figure 4b. From the figure, it is seen that the $f_{app}Re$ has a rapid reduction with an increase in ξ and the $f_{app}Re$ at the entrance region is significantly higher than the fully developed values of fRe. The $f_{app}Re$ is found to be sensitive to low Reynolds numbers. Moreover, the $f_{app}Re$ at low Reynolds numbers is markedly higher than the values at high Reynolds numbers, especially in the entrance region.

The variations of the frictional entropy generation rate with different Re numbers are shown in Figure 5. It can be seen that for a given volume fraction of Al_2O_3–water nanofluid, the frictional entropy generation rate dramatically increases by increasing the Reynolds number. When the Reynolds number increases from 100 to 200, the frictional entropy generation rate increases approximately by three times. Moreover, when the Reynolds number increases from 500 to 1000, the frictional entropy generation rate of the channel increases by 389%. This increment is significant at higher values of Reynolds number. An increase in the flow velocity of the working fluid leads to the increase in the flow resistance so that more pressure energy needs to be supplied to drive the flow in MCHS, which increases the frictional dissipation and irreversibility, leading to a significant increase in entropy generation. In addition, the addition of nanoparticles in the working fluid further increases the entropy generation. It is observed that the higher entropy generation gradient in the entry region, which displays the entrance effects.
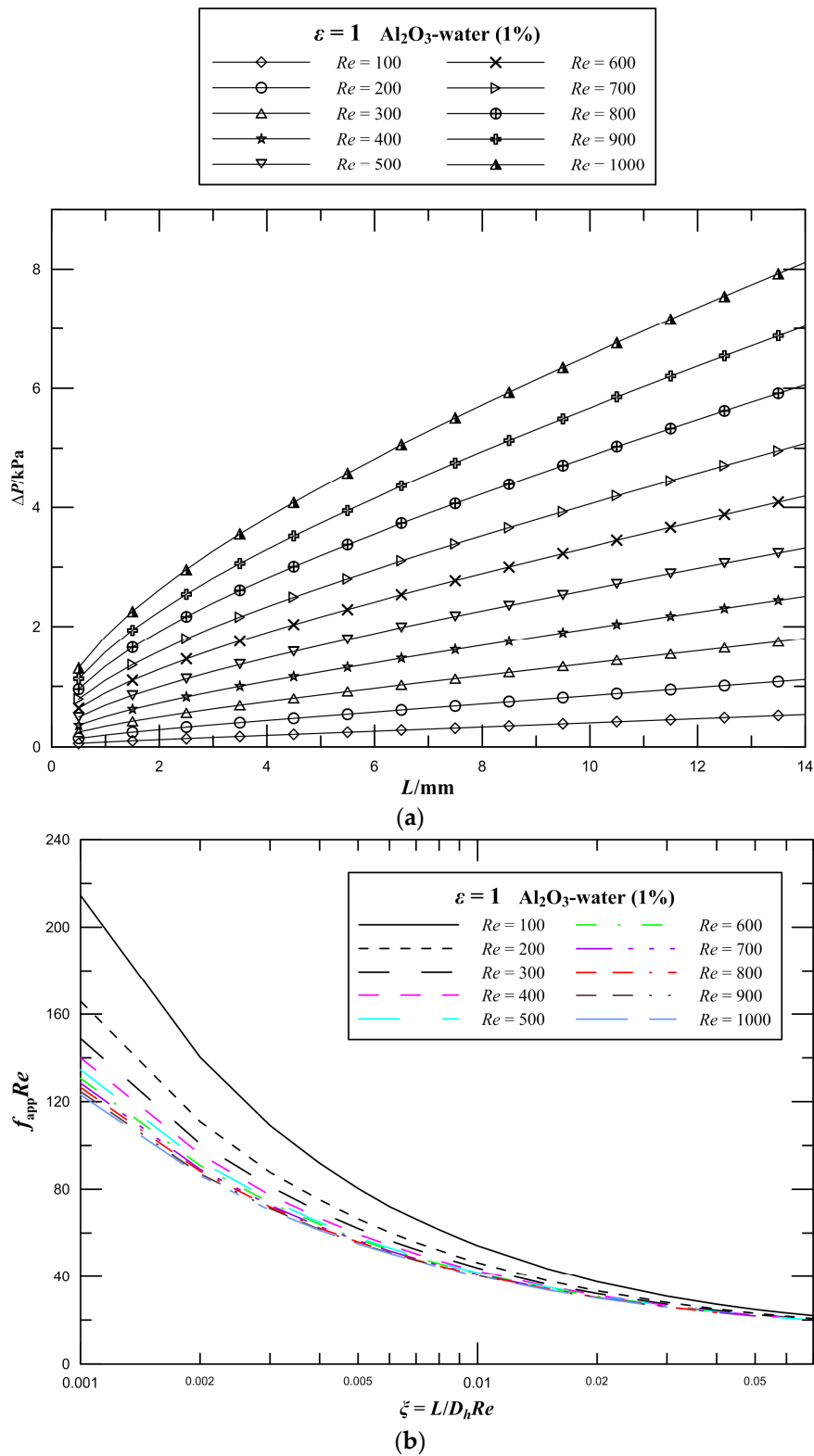
Figure 4. Effect of Reynolds number on flow parameters for rectangular channels. (**a**) Pressure drop; (**b**) $f_{app}Re$.
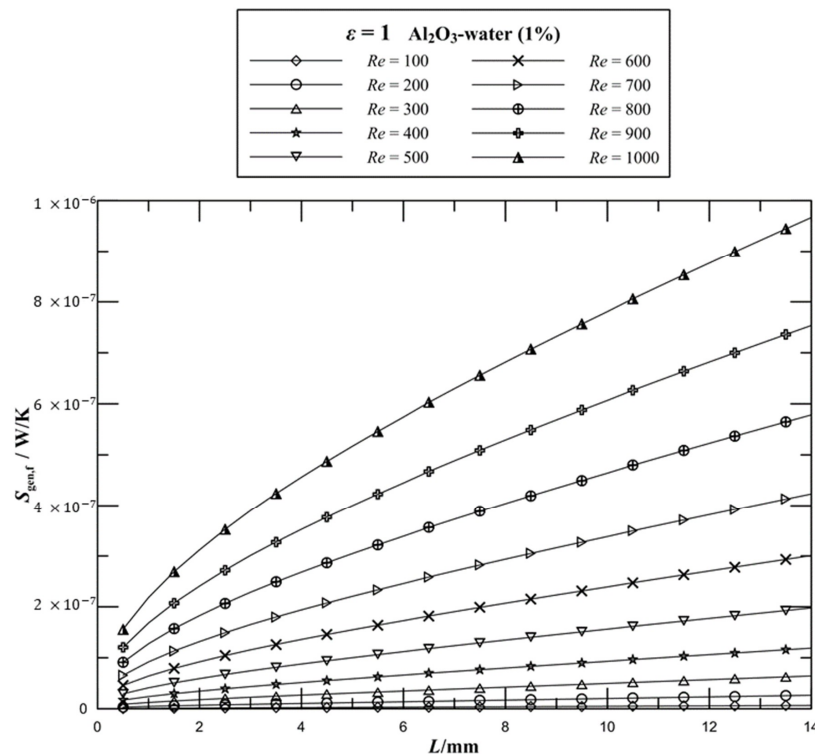
Figure 5. Effect of Reynolds number on the frictional entropy generation rate for rectangular channels.

4.3. Effect of Aspect Ratio on Pressure Drop and Frictional Entropy Generation

For the 1 vol.% Al_2O_3–water nanofluid, three-dimensional numerical simulations of rectangular microchannel heat sinks with various aspect ratios were conducted at a Reynolds number of 500. Figure 6a illustrates the pressure drop of microchannel heat sinks with aspect ratios ranging from 0.1 to 1. As can be observed, the pressure drop monotonically increases along the flow direction in the microchannel heat sink, and the pressure drop slightly increases as the aspect ratio decreases for the same Reynolds number. The pressure drop of the channel is higher at lower values of ε. In detail, when the aspect ratio increases from 0.6 to 1, the pressure drop of the channel decreases by 2%; however, when the aspect ratio increases from 0.1 to 0.5, the pressure drop of the channel decreases by 15%. This is because as the aspect ratio increases, the circumferential area of rectangular microchannels decreases, that is, the contact area of the working fluid with the walls of the channels decreases. Thus, the flow resistance decreases, which results in a slight decrease in the pressure drop. Especially at low aspect ratios, the reduction in the contact area is greater. Likewise, it is observed that the higher pressure gradient in the entrance region of rectangular channels. In the entrance region, the high velocity gradient at the wall results in a high shear stress and the high pressure gradient needed to produce the high acceleration in the near wall region.

The effect of aspect ratio on $f_{app}Re$ values of laminar flow in microchannel plate fin heat sinks is illustrated in Figure 6b. There is a great reduction in $f_{app}Re$ where ξ is less than 0.04, and subsequently $f_{app}Re$ tends to a certain value. It is observed that the effect of aspect ratio on $f_{app}Re$ values is evident when ξ is greater than 0.04, and the influence increases by increasing ξ. The effect of aspect ratio on the frictional entropy generation rate is presented in Figure 7. It is noted that the frictional entropy generation rate is higher for lower aspect ratios. The frictional entropy generation rate decreases with increasing ε. The influence of aspect ratio on the frictional entropy generation rate is unobvious at larger aspect ratios. Figures 6 and 7 illustrate that the pressure drop and frictional entropy generation are not observably affected by the aspect ratio at the entrance region. The reason is the variation in the contact area caused by the change in the aspect ratio has not yet worked at the entry region, and as the length of the channels increases, the effect of the aspect ratio is accumulated and displayed.
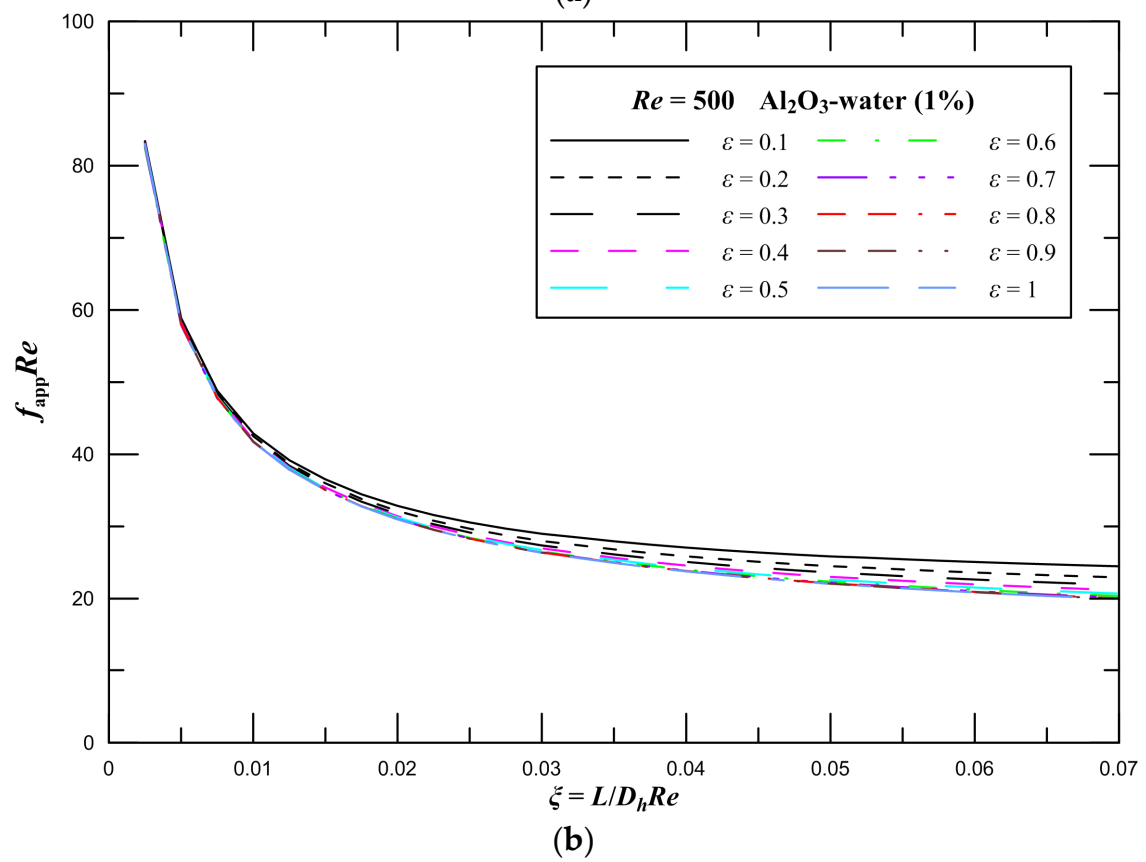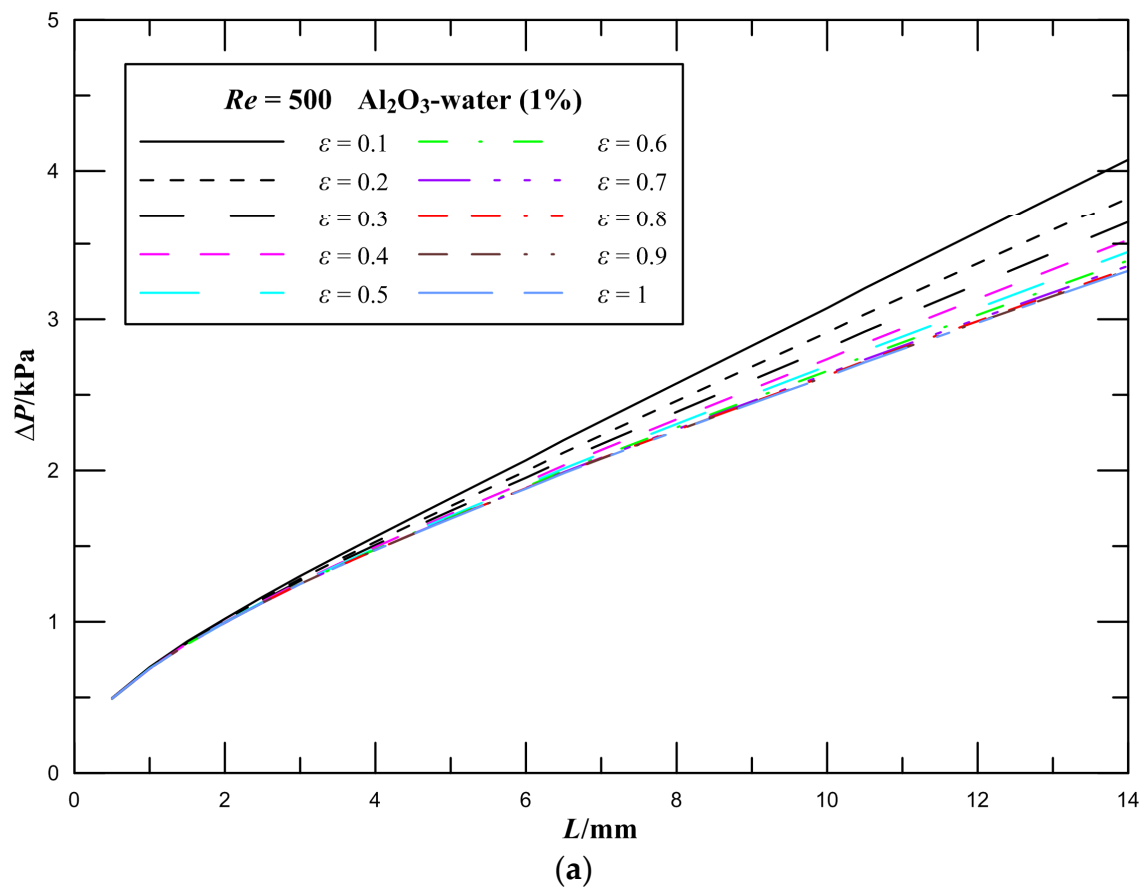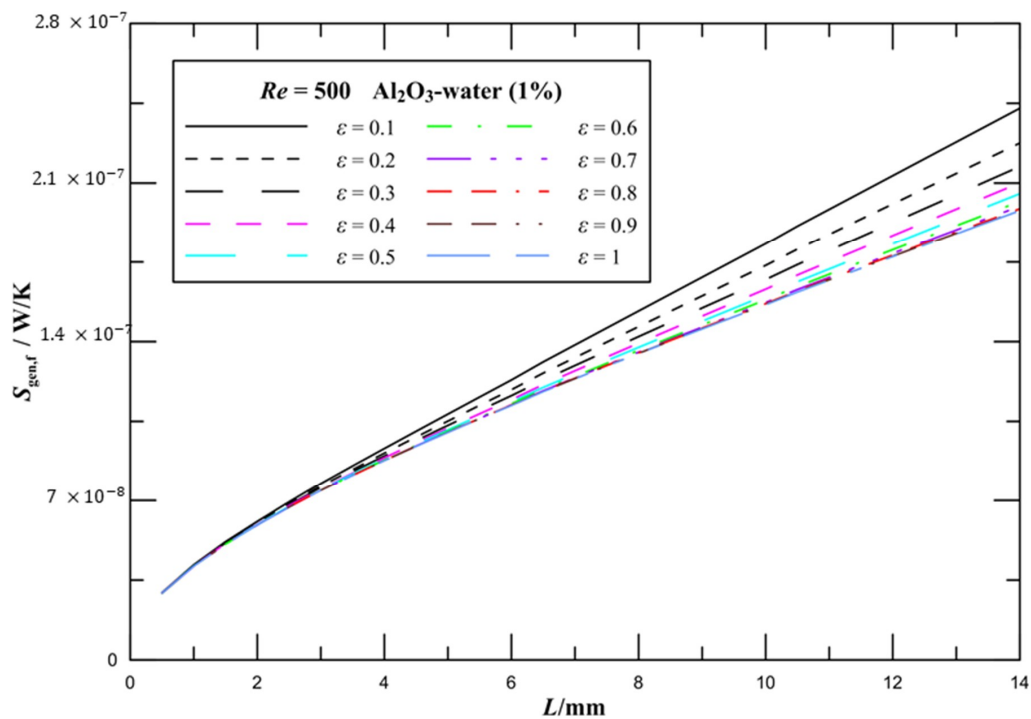
**Figure 6.** Effect of aspect ratio on flow parameters for rectangular channels. (**a**) Pressure drop; (**b**) $f_{app}Re$.

Figure 7. Effect of aspect ratio on the frictional entropy generation rate for rectangular channels.

4.4. Effect of Volume Fraction of Al_2O_3-water Nanofluid on Pressure Drop and Frictional Entropy Generation

Numerical simulations of fluid flow in microchannel plate fin heat sinks using 0, 0.5, 1, 3, and 5 vol.% Al_2O_3–water nanofluid at $Re = 200$ and $\varepsilon = 1$, $Re = 500$ and $\varepsilon = 0.5$, and $Re = 1000$ and $\varepsilon = 0.2$ were carried out. Figure 8a–c illustrates the variations of the pressure drop parameter along the streamwise direction in rectangular ducts at different nanoparticle volume fractions. It is seen that the pressure drop increases along the flow direction in the microchannel heat sink, and the pressure drop slightly increases as nanoparticle volume fraction increases for the same aspect ratio. In detail, when the nanoparticle volume fraction increases from 0 to 1% at $Re = 500$, the pressure drop of rectangular microchannel heat sinks with the aspect ratio $\varepsilon = 0.5$ increases by 3%. Further, when the nanoparticle volume fraction increases from 1 to 5%, the pressure drop of the channel increases by 12%. The effect of increasing the nanoparticle concentration is to increase the pressure drop of the channel. In addition, it is obvious that the higher pressure gradient occurs when L is just less than 4 mm, and the pressure drop increases linearly later along the flow direction in channels for the same Reynolds number, especially in the lower aspect ratio and higher Reynolds number. The higher pressure gradient is caused by the momentum flux variation due to the change of velocity field from a uniform profile at the inlet to a specific profile downstream in the channel.

The frictional entropy generation characteristics of rectangular microchannel heat sinks with the aspect ratio $\varepsilon = 1$ at a Reynolds number of 200 were presented in Figure 8d. As can be observed, the viscous entropy generation increases mildly by increasing the nanoparticle volume fraction. When the nanoparticle volume fraction increases from 0 to 1%, the viscous entropy generation of the channel increases by 3%. Further, when the nanoparticle volume fraction increases from 0 to 5%, the viscous entropy generation of the channel increases by 17%. High nanoparticle volume fraction causes better heat transfer performance as well as higher entropy generation. The reason is that the viscosity increases with an increase in the concentration, which intensifies the frictional entropy generation and pressure drop. The contribution of the developing region plays a key role in determining the variations of the frictional entropy generation and pressure drop.

(**a**)

(**b**)

(**c**)

(**d**)
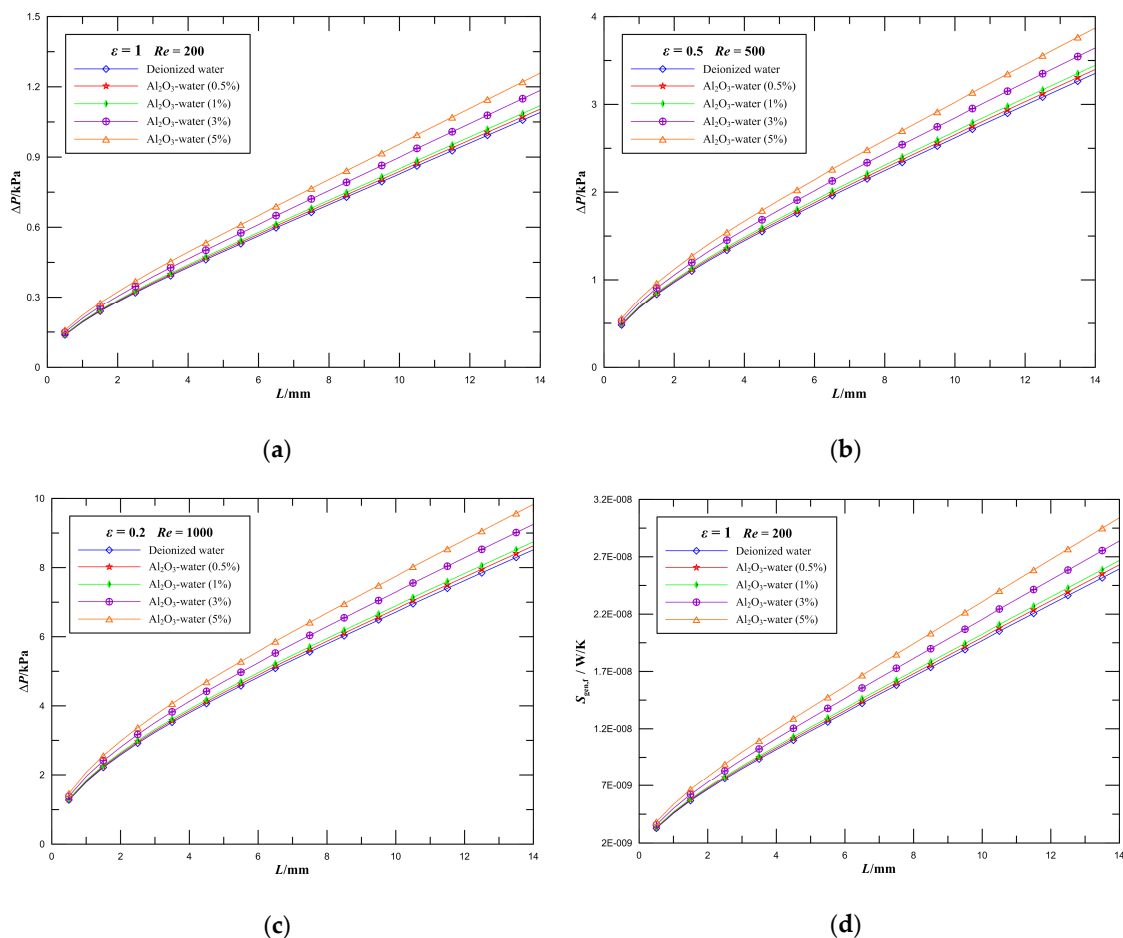
Figure 8. Effect of nanoparticle volume fraction on pressure drop and frictional entropy generation rate. (**a**) Pressure drop of rectangular microchannel heat sinks with $\varepsilon = 1$ at $Re = 200$; (**b**) Pressure drop of rectangular microchannel heat sinks with $\varepsilon = 0.5$ at $Re = 500$; (**c**) Pressure drop of rectangular microchannel heat sinks with $\varepsilon = 0.2$ at $Re = 1000$; (**d**) Frictional entropy generation rate of rectangular microchannel heat sinks with $\varepsilon = 1$ at $Re = 200$.

Figure 9 demonstrates the comparison of the Fanning friction factor between the current results and the available experimental results from Karimzadehkhouei et al. [66], Hussien et al. [68], Jung et al. [80], Lee and Mudawar [81], Ho et al. [82], Hussien et al. [83], and Peyghambarzadeh et al. [84]. It is observed that our results agree favorably with the experimental data reported by Karimzadehkhouei et al. [66], Lee and Mudawar [81], Ho et al. [82], and Hussien et al. [83], and our results are close to the available analytical data from Duan and Muzychka [76]. Most of the experimental data from Peyghambarzadeh et al. [84] are close to the theoretical solution. The measured values of the friction factor from Jung et al. [80] are larger than those predicted by the theoretical solution. The deviation is most likely due to entrance effects, and possibly due to measuring experimental error and channel surface roughness effects caused by the fabrication technique. Therefore, it is necessary to pay attention to entrance effects, especially in short microchannel heat sinks. Lee and Mudawar [81] and Ho et al. [82] experimentally studied the convective heat transfer and fluid flow of Al_2O_3–water nanofluid in rectangular microchannels with the aspect ratio $\varepsilon = 0.26$ and $\varepsilon = 0.35$, respectively, and it is seen that their results agree well with the analytical solution of rectangular microchannels with the aspect ratio $\varepsilon = 0.3$ from Duan and Muzychka [76]. The experiments of fluid flow in a circular mini-tube were carried out by Hussien et al. [83] employing multi-walled carbon nanotubes (MWCNTs)/water nanofluids, and as seen from this graph, the measured results are close to the fully developed friction factor $f = 16/Re$ of the theoretical solution of circular tubes.
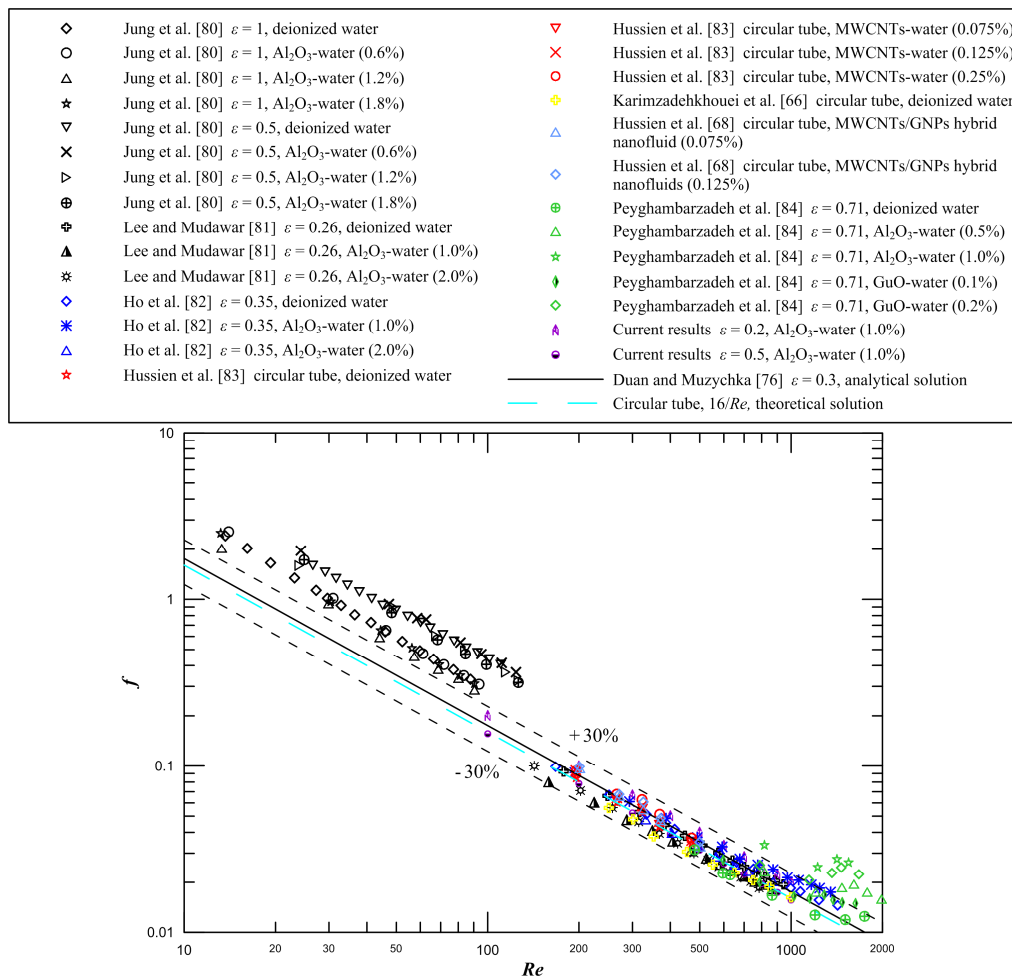
◇	Jung et al. [80] $\varepsilon = 1$, deionized water		▽	Hussien et al. [83] circular tube, MWCNTs-water (0.075%)
○	Jung et al. [80] $\varepsilon = 1$, Al₂O₃-water (0.6%)		✕	Hussien et al. [83] circular tube, MWCNTs-water (0.125%)
△	Jung et al. [80] $\varepsilon = 1$, Al₂O₃-water (1.2%)		○	Hussien et al. [83] circular tube, MWCNTs-water (0.25%)
★	Jung et al. [80] $\varepsilon = 1$, Al₂O₃-water (1.8%)		✛	Karimzadehkhouei et al. [66] circular tube, deionized water
▽	Jung et al. [80] $\varepsilon = 0.5$, deionized water		△	Hussien et al. [68] circular tube, MWCNTs/GNPs hybrid nanofluid (0.075%)
✕	Jung et al. [80] $\varepsilon = 0.5$, Al₂O₃-water (0.6%)		◇	Hussien et al. [68] circular tube, MWCNTs/GNPs hybrid nanofluids (0.125%)
▷	Jung et al. [80] $\varepsilon = 0.5$, Al₂O₃-water (1.2%)		⊕	Peyghambarzadeh et al. [84] $\varepsilon = 0.71$, deionized water
⊕	Jung et al. [80] $\varepsilon = 0.5$, Al₂O₃-water (1.8%)		△	Peyghambarzadeh et al. [84] $\varepsilon = 0.71$, Al₂O₃-water (0.5%)
⊕	Lee and Mudawar [81] $\varepsilon = 0.26$, deionized water		★	Peyghambarzadeh et al. [84] $\varepsilon = 0.71$, Al₂O₃-water (1.0%)
▲	Lee and Mudawar [81] $\varepsilon = 0.26$, Al₂O₃-water (1.0%)		◓	Peyghambarzadeh et al. [84] $\varepsilon = 0.71$, GuO-water (0.1%)
✳	Lee and Mudawar [81] $\varepsilon = 0.26$, Al₂O₃-water (2.0%)		◇	Peyghambarzadeh et al. [84] $\varepsilon = 0.71$, GuO-water (0.2%)
◇	Ho et al. [82] $\varepsilon = 0.35$, deionized water		▲	Current results $\varepsilon = 0.2$, Al₂O₃-water (1.0%)
✳	Ho et al. [82] $\varepsilon = 0.35$, Al₂O₃-water (1.0%)		●	Current results $\varepsilon = 0.5$, Al₂O₃-water (1.0%)
△	Ho et al. [82] $\varepsilon = 0.35$, Al₂O₃-water (2.0%)		———	Duan and Muzychka [76] $\varepsilon = 0.3$, analytical solution
★	Hussien et al. [83] circular tube, deionized water		– – –	Circular tube, 16/*Re*, theoretical solution

Figure 9. Comparison of the friction factor for current results and experimental results from the literature.

It can be seen that the current results and most of the experimental data agree with the analytical solution from Duan and Muzychka [76] within ±30%. To account for this discrepancy, a careful analysis of the experimental uncertainty is performed in this study. A basic equation of uncertainty analysis was presented by Moffat [85] utilizing the root sum square method and the equation can be expressed as

$$U_R = \sqrt{\sum_{i=1}^{n}\left(\frac{\partial R}{\partial x_i} U_i\right)^2} \qquad (23)$$

where R is the evaluation object, x_i is a variable in R, and U_i is the uncertainty of the variable x_i. The friction factor can be expressed as follows

$$f = \frac{\Delta P D_h}{2\rho u_m^2 L} \qquad (24)$$

According to Equation (10), the experimental uncertainties in f are given as

$$\frac{U_f}{f} = \left[\left(\frac{U_{\Delta P}}{\Delta P}\right)^2 + \left(\frac{U_{D_h}}{D_h}\right)^2 + \left(\frac{U_\rho}{\rho}\right)^2 + 2\left(\frac{U_{u_m}}{u_m}\right)^2 + \left(\frac{U_L}{L}\right)^2\right]^{1/2} \qquad (25)$$

From Equation (25), it is seen that the uncertainties in f are the measurements of the pressure drop, microchannel hydrodynamic diameter, density, flow velocity, and channel length. It is extremely difficult to accurately measure the dimension of microchannels, particularly when the dimensions reach microscale levels. In addition, entrance effects and channel surface roughness effects caused by the fabrication technique play an important role in the experimental uncertainties.

5. Conclusions

A three-dimensional numerical study of the flow characteristics of nanofluids in microchannel plate fin heat sinks considering entrance effects has been carried out in this paper. The effects of the Reynolds number, channel aspect ratio, and nanofluid volume fraction on pressure drop and entropy generation in microchannel plate fin heat sinks were analyzed in detail. In light of the preceding discussions, we draw the following conclusions.

(1) For given nanoparticle volume fraction and channel aspect ratio, the frictional entropy generation and pressure drop of the microchannel plate fin heat sinks dramatically increase by increasing the Reynolds number. For the 1 vol.% Al_2O_3–water nanofluid, when the Reynolds number increases from 500 to 1000, the pressure drop and frictional entropy generation of rectangular microchannel heat sinks with aspect ratio $\varepsilon = 1$ increases by 144% and 389%, respectively. In addition, the $f_{app}Re$ at low Reynolds numbers is higher than the values at high Reynolds numbers, especially in the entrance region.

(2) The frictional entropy generation and pressure drop slightly increases as the channel aspect ratio decreases. For the 1 vol.% Al_2O_3–water nanofluid, when the aspect ratio increases from 0.6 to 1 at $Re = 500$, the pressure drop of the channel decreases by 2%; however, when the aspect ratio increases from 0.1 to 0.5, the pressure drop of the channel decreases by 15%. The results also demonstrate that the flow parameters are not observably affected by the geometry of the cross-section at the entrance region.

(3) Given an increase in nanoparticle volume fraction, the frictional entropy generation and pressure drop have a slight increase. When the nanoparticle volume fraction increases from 0 to 1% at $Re = 500$, the pressure drop of microchannel plate fin heat sinks with the aspect ratio $\varepsilon = 0.5$ increases by 3%. Further, when the nanoparticle volume fraction increases from 1 to 5%, the pressure drop of the channel increases by 12%. The results mean that a heat transfer enhancement can be obtained by adding appropriate volume fraction of nanoparticles in a base fluid without significantly increasing pump work.

(4) The higher viscous entropy generation rate gradient and significantly higher $f_{app}Re$ values occur in the entrance region, which indicates the critical importance of the effect of the entry region in determining the behavior of microchannel heat sinks. Furthermore, the general expression of the entropy generation rate considering entrance effects is developed.

In future research work, we will further study the cooling performance of microchannel plate fin heat sinks with different nanofluids as coolants employing entropy generation minimization method.

Author Contributions: Conceptualization, H.M. and Z.D.; Methodology, H.M. and Z.D.; Software, H.M., L.S., and X.N.; Validation, J.B. and X.L.; Writing—Original draft, H.M.; Writing—Review & Editing, Z.D.

Conflicts of Interest: The authors declare no conflicts of interest.

Nomenclature

a	major semi-axis of rectangle, μm
A	flow area, m^2
b	minor semi-axis of rectangle, μm
Cp	specific heat capacity at constant pressure, J/(kg·K)
d_p	particle diameter, nm
D_h	hydraulic diameter, $= 4A/P$
f	Fanning friction factor, $= \bar{\tau}/\left(\frac{1}{2}\rho u_m^2\right)$
H	height of heat sinks, mm
k	thermal conductivity, W/(m·K)
L	length of heat sinks, mm
p	pressure, N/m^2
Po	Poiseuille number, $= \bar{\tau}D_h/\mu u_m$
Pr	Prandtl number,$= \mu Cp/k$
$\dot{Q}$	heat transfer rate, W
R	evaluation object
Re	Reynolds number, $= u_m D_h/\nu$
$\dot{S}'''_{gen}$	local entropy generation rate, W/(m^3·K)
$\dot{S}_{gen}$	global entropy generation rate, W/K
t	fin thickness, m
T	temperature, K
u	velocity, m/s
u_m	average velocity, m/s
U	velocity scale, m/s
U_i	uncertainty of the variable x_i
W	width of heat sinks, mm
x, y	Cartesian coordinates, m
x_i	independent variable
z	coordinate in flow direction, m
Greek symbols	
ε	aspect ratio, $= b/a$
μ	dynamic viscosity, N·s/m^2
ν	kinematic viscosity, m^2/s
ξ	dimensionless hydrodynamic channel length, $= L/(D_h Re)$
ρ	density, kg/m^3
$\bar{\tau}$	wall shear stress, N/m^2
ϕ	nanoparticle volume fraction, %
Subscripts	
a	ambient
b	heat sink base surface
bf	base fluid
D_h	based upon the hydraulic diameter
m	mean
nf	nanofluid
p	nanoparticle

References

1. Ma, N.Y.; Duan, Z.P.; Ma, H.; Su, L.B.; Liang, P.; Ning, X.R.; He, B.S.; Zhang, X. Lattice Boltzmann simulation of the hydrodynamic entrance region of rectangular microchannels in the slip regime. *Micromachines* **2018**, *9*, 87. [CrossRef] [PubMed]
2. Wang, S.X.; Yin, Y.; Hu, C.X.; Rezai, P. 3D integrated circuit cooling with microfluidics. *Micromachines* **2018**, *9*, 287. [CrossRef] [PubMed]

3. Duan, Z.P.; Ma, H.; He, B.S.; Su, L.B.; Zhang, X. Pressure drop of microchannel plate fin heat sinks. *Micromachines* **2019**, *10*, 80. [CrossRef] [PubMed]

4. Adham, A.M.; Mohd-Ghazali, N.; Ahmad, R. Thermal and hydrodynamic analysis of microchannel heat sinks: A review. *Renew. Sustain. Energy Rev.* **2013**, *21*, 614–622. [CrossRef]

5. Colin, S. Gas microflows in the slip flow regime: A critical review on convective heat transfer. *Trans. ASME J. Heat Transf.* **2012**, *134*, 020908. [CrossRef]

6. Duan, Z.P.; Muzychka, Y.S. Slip flow in elliptic microchannels. *Int. J. Therm. Sci.* **2007**, *46*, 1104–1111. [CrossRef]

7. Morini, G.L. Scaling effects for liquid flows in microchannels. *Heat Transf. Eng.* **2006**, *27*, 64–73. [CrossRef]

8. Liu, D.; Garimella, S.V. Investigation of liquid flow in microchannels. *J. Thermophys. Heat Transf.* **2004**, *18*, 65–72. [CrossRef]

9. Kong, K.S.; Ooi, K.T. A numerical and experimental investigation on microscale heat transfer effect in the combined entry region in macro geometries. *Int. J. Therm. Sci.* **2013**, *68*, 8–19. [CrossRef]

10. Wang, C.Y. On the Nusselt number for H2 heat transfer in rectangular ducts of large aspect ratios. *Trans. ASME J. Heat Transf.* **2014**, *136*, 074501. [CrossRef]

11. Wang, C.Y. Mixed H1 and H2 forced convection in a rectangular duct. *Trans. ASME J. Heat Transf.* **2018**, *140*, 034502. [CrossRef]

12. Vocale, P.; Morini, G.L.; Spiga, M. Convective heat transfer in elliptical microchannels under slip flow regime and h1 boundary conditions. *Trans. ASME J. Heat Transf.* **2016**, *138*, 044502. [CrossRef]

13. Si Salah, S.A.; Filali, E.G.; Djellouli, S. Numerical investigation of Reynolds number and scaling effects in microchannels flows. *J. Hydrodyn.* **2017**, *29*, 647–658. [CrossRef]

14. Cheng, K.X.; Chong, Y.S.; Ooi, K.T. Thermal-hydraulic performance of a tapered microchannel. *Int. Commun. Heat Mass Transf.* **2018**, *94*, 53–60. [CrossRef]

15. Steinke, M.E.; Kandlikar, S.G. Single-phase liquid friction factors in microchannels. *Int. J. Therm. Sci.* **2006**, *45*, 1073–1083. [CrossRef]

16. Wen, D.S.; Ding, Y.L. Experimental investigation into convective heat transfer of nanofluids at the entrance region under laminar flow conditions. *Int. J. Heat Mass Transf.* **2004**, *47*, 5181–5188. [CrossRef]

17. Mishan, Y.; Mosyak, A.; Pogrebnyak, E.; Hetsroni, G. Effect of developing flow and thermal regime on momentum and heat transfer in micro-scale heat sink. *Int. J. Heat Mass Transf.* **2007**, *50*, 3100–3114. [CrossRef]

18. Bayraktar, T.; Pidugu, S.B. Characterization of liquid flows in microfluidic systems. *Int. J. Heat Fluid Flow* **2006**, *49*, 815–824. [CrossRef]

19. Vocale, P.; Spiga, M. Slip flow in the hydrodynamic entrance region of microchannels. *Int. J. Microscale Nanoscale Therm. Fluid Transp. Phenom.* **2013**, *4*, 175–191.

20. Renksizbulut, M.; Niazmand, H.; Tercan, G. Slip-flow and heat transfer in rectangular microchannels with constant wall temperature. *Int. J. Therm. Sci.* **2006**, *45*, 870–881. [CrossRef]

21. Hettiarachchi, H.D.M.; Golubovic, M.; Worek, W.M.; Minkowycz, W.J. Three-dimensional laminar slip-flow and heat transfer in a rectangular microchannel with constant wall temperature. *Int. J. Heat Mass Transf.* **2008**, *51*, 5088–5096. [CrossRef]

22. Hamadneh, N.N.; Khan, W.A.; Khan, I.; Alsagri, A.S. Modeling and optimization of gaseous thermal slip flow in rectangular microducts using a particle swarm optimization algorithm. *Symmetry* **2019**, *11*, 488. [CrossRef]

23. Pang, L.P.; Wang, M.X.; Wang, W.; Liu, M.; Wang, J. Optimal thermal design of a stacked mini-channel heat sink cooled by a low flow rate coolant. *Entropy* **2013**, *15*, 4716–4731. [CrossRef]

24. Vinodhan, V.L.; Rajan, K.S. Computational analysis of new microchannel heat sink configurations. *Energy Convers. Manag.* **2014**, *86*, 595–604. [CrossRef]

25. Lu, S.N.; Vafai, K. A comparative analysis of innovative microchannel heat sinks for electronic cooling. *Int. Commun. Heat Mass Transf.* **2016**, *76*, 271–284. [CrossRef]

26. Wang, R.J.; Wang, W.; Wang, J.W.; Zhu, Z.F. Analysis and optimization of trapezoidal grooved microchannel heat sink using nanofluids in a micro solar cell. *Entropy* **2017**, *20*, 9. [CrossRef]

27. Ansari, D.; Kim, K.-Y. Performance analysis of double-layer microchannel heat sinks under non-uniform heating conditions with random hotspots. *Micromachines* **2017**, *8*, 54. [CrossRef]

28. Jing, D.L.; Song, S.Y.; Pan, Y.L.; Wang, X.M. Size dependences of hydraulic resistance and heat transfer of fluid flow in elliptical microchannel heat sinks with boundary slip. *Int. J. Heat Mass Transf.* **2018**, *119*, 647–653. [CrossRef]

29. Jing, D.L.; He, L. Thermal characteristics of staggered double-layer microchannel heat sink. *Entropy* **2018**, *20*, 537. [CrossRef]

30. Radwan, A.; Ookawara, S.; Mori, S.; Ahmed, M. Uniform cooling for concentrator photovoltaic cells and electronic chips by forced convective boiling in 3D-printed monolithic double-layer microchannel heat sink. *Energy Convers. Manag.* **2018**, *166*, 356–371. [CrossRef]

31. Soleimanikutanaei, S.; Ghasemisahebi, E.; Lin, C.-X. Numerical study of heat transfer enhancement using transverse microchannels in a heat sink. *Int. J. Therm. Sci.* **2018**, *125*, 89–100. [CrossRef]

32. Al Siyabi, I.; Khanna, S.; Sundaram, S.; Mallick, T. Experimental and numerical thermal analysis of multi-layered microchannel heat sink for concentrating photovoltaic application. *Energies* **2019**, *12*, 122. [CrossRef]

33. Deng, D.X.; Pi, G.; Zhang, W.X.; Wang, P.; Fu, T. Numerical study of double-layered microchannel heat sinks with different cross-sectional shapes. *Entropy* **2019**, *21*, 16. [CrossRef]

34. Xie, X.L.; Liu, Z.J.; He, Y.L.; Tao, W.Q. Numerical study of laminar heat transfer and pressure drop characteristics in a water-cooled minichannel heat sink. *Appl. Therm. Eng.* **2009**, *29*, 64–74. [CrossRef]

35. Hung, T.-C.; Yan, W.-M. Enhancement of thermal performance in double-layered microchannel heat sink with nanofluids. *Int. J. Heat Mass Transf.* **2012**, *55*, 3225–3238. [CrossRef]

36. Hung, T.-C.; Yan, W.-M.; Wang, X.-D.; Chang, C.-Y. Heat transfer enhancement in microchannel heat sinks using nanofluids. *Int. J. Heat Mass Transf.* **2012**, *55*, 2559–2570. [CrossRef]

37. Nasiri, M.; Rashidi, M.M.; Lorenzini, G. Effect of magnetic field on entropy generation in a microchannel heat sink with offset fan shaped. *Entropy* **2016**, *18*, 10. [CrossRef]

38. Bahiraei, M.; Heshmatian, S. Thermal performance and second law characteristics of two new microchannel heat sinks operated with hybrid nanofluid containing grapheme-silver nanoparticles. *Energy Convers. Manag.* **2018**, *168*, 357–370. [CrossRef]

39. Xia, G.D.; Liu, R.; Wang, J.; Du, M. The characteristics of convective heat transfer in microchannel heat sinks using Al_2O_3 and TiO_2 nanofluids. *Int. Commun. Heat Mass Transf.* **2016**, *76*, 256–264. [CrossRef]

40. Hassani, S.M.; Khoshvaght-Aliabadi, M.; Mazloumi, S.H. Influence of chevron fin interruption on thermo-fluidic transport characteristics of nanofluid-cooled electronic heat sink. *Chem. Eng. Sci.* **2018**, *191*, 436–447. [CrossRef]

41. Sarafraz, M.M.; Nikkhah, V.; Nakhjavani, M.; Arya, A. Thermal performance of a heat sink microchannel working with biologically produced silver-water nanofluid: Experimental assessment. *Exp. Therm. Fluid Sci.* **2018**, *91*, 509–519. [CrossRef]

42. Fan, Y.; Lee, P.S.; Jin, L.-W.; Chua, B.W. Experimental investigation on heat transfer and pressure drop of a novel cylindrical oblique fin heat sink. *Int. J. Therm. Sci.* **2014**, *76*, 1–10. [CrossRef]

43. Kanargi, B.; Lee, P.S.; Yap, C. A numerical and experimental investigation of heat transfer and fluid flow characteristics of an air-cooled oblique-finned heat sink. *Int. J. Heat Mass Transf.* **2018**, *116*, 393–416. [CrossRef]

44. Xu, F.; Wu, H.Y. Experimental study of water flow and heat transfer in silicon micro-pin-fin heat sinks. *Trans. ASME J. Heat Transf.* **2018**, *140*, 122401. [CrossRef]

45. Milanese, M.; Iacobazzi, F.; Colangelo, G.; de Risi, A. An investigation of layering phenomenon at the liquid-solid interface in Cu and CuO based nanofluids. *Int. J. Heat Mass Transf.* **2016**, *103*, 564–571. [CrossRef]

46. Iacobazzi, F.; Milanese, M.; Colangelo, G.; Lomascolo, M.; de Risi, A. An explanation of the Al_2O_3 nanofluid thermal conductivity based on the phonon theory of liquid. *Energy* **2016**, *116*, 786–794. [CrossRef]

47. Iacobazzi, F.; Milanese, M.; Colangelo, G.; de Risi, A. A critical analysis of clustering phenomenon in Al_2O_3 nanofluids. *J. Therm. Anal. Calorim.* **2019**, *135*, 371–377. [CrossRef]

48. Duan, Z.P.; He, B.S.; Duan, Y.Y. Sphere drag and heat transfer. *Sci. Rep.* **2015**, *5*, 12304. [CrossRef]

49. Chai, L.; Wang, L.; Bai, X. Thermohydraulic performance of microchannel heat sinks with triangular ribs on sidewalls–Part 1: Local fluid flow and heat transfer characteristics. *Int. J. Heat Mass Transf.* **2018**, *127*, 1124–1137. [CrossRef]

50. Khan, A.A.; Kim, S.M.; Kim, K.-Y. Performance analysis of a microchannel heat sink with various rib configurations. *J. Thermophys. Heat Transf.* **2015**, *30*, 782–790. [CrossRef]

51. Chai, L.; Xia, G.D.; Wang, H.S. Laminar flow and heat transfer characteristics of interrupted microchannel heat sink with ribs in the transverse microchambers. *Int. J. Therm. Sci.* **2016**, *110*, 1–11. [CrossRef]

52. Bejan, A. A study of entropy generation in fundamental convective heat transfer. *Trans. ASME J. Heat Transf.* **1979**, *101*, 718–725. [CrossRef]

53. Bejan, A. Entropy generation minimization: The new thermodynamics of finite-size devices and finite-time processes. *J. Appl. Phys.* **1996**, *79*, 1191–1218. [CrossRef]

54. Wu, J.; Guo, Z.-Y. Entropy and its correlations with other related quantities. *Entropy* **2014**, *16*, 1089–1100. [CrossRef]

55. Hua, Y.-C.; Zhao, T.; Guo, Z.-Y. Irreversibility and action of the heat conduction process. *Entropy* **2018**, *20*, 206.

56. Zhao, T.; Hua, Y.-C.; Guo, Z.-Y. The principle of least action for reversible thermodynamic processes and cycles. *Entropy* **2018**, *20*, 542. [CrossRef]

57. Eger, T.; Bol, T.; Thanu, A.; Daróczy, L.; Janiga, G.; Schroth, R.; Thévenin, D. Application of entropy generation to improve heat transfer of heat sinks in electric machines. *Entropy* **2017**, *19*, 255. [CrossRef]

58. Bondarenko, D.S.; Sheremet, M.A.; Oztop, H.F.; Ali, M.E. Impacts of moving wall and heat-generating element on heat transfer and entropy generation of Al_2O_3/H_2O nanofluid. *J. Therm. Anal. Calorim.* **2019**, *136*, 673–686. [CrossRef]

59. Khan, W.A.; Culham, J.R.; Yovanovich, M.M. Optimization of microchannel heat sinks using entropy generation minimization method. *IEEE Trans. Compon. Package Technol.* **2009**, *32*, 243–251. [CrossRef]

60. Awad, M.M. A review of entropy generation in microchannels. *Adv. Mech. Eng.* **2015**, *7*, 1687814015590297. [CrossRef]

61. Hassan, M.; Sadri, R.; Ahmadi, G.; Dahari, M.B.; Kazi, S.N.; Safaei, M.R.; Sadeghinezhad, E. Numerical study of entropy generation in a flowing nanofluid used in micro-and minichannels. *Entropy* **2013**, *15*, 144–155. [CrossRef]

62. Abbas, M.A.; Bai, Y.; Rashidi, M.M.; Bhatti, M.M. Analysis of entropy generation in the flow of peristaltic nanofluids in channels with compliant walls. *Entropy* **2016**, *18*, 90. [CrossRef]

63. Bhatti, M.M.; Abbas, T.; Rashidi, M.M.; Ali, M.E.-S. Numerical simulation of entropy generation with thermal radiation on MHD Carreau nanofluid towards a shrinking sheet. *Entropy* **2016**, *18*, 200. [CrossRef]

64. Ji, Y.; Zhang, H.-C.; Yang, X.; Shi, L. Entropy generation analysis and performance evaluation of turbulent forced convective heat transfer to nanofluids. *Entropy* **2017**, *19*, 108. [CrossRef]

65. Rashidi, M.M.; Abbas, M.A. Effect of slip conditions and entropy generation analysis with an effective Prandtl number model on a nanofluid flow through a stretching sheet. *Entropy* **2017**, *19*, 414. [CrossRef]

66. Karimzadehkhouei, M.; Shojaeian, M.; Sadaghiani, A.; Şendur, K.; Mengüç, M.; Koşar, A. Entropy generation analysis of laminar flows of water-based nanofluids in horizontal minitubes under constant heat flux conditions. *Entropy* **2018**, *20*, 242. [CrossRef]

67. Lorenzini, G.; Mahian, O. Entropy in Nanofluids. *Entropy* **2018**, *20*, 339. [CrossRef]

68. Hussien, A.A.; Abdullah, M.Z.; Yusop, N.M.; Al-Kouz, W.; Mahmoudi, E.; Mehrali, M. Heat transfer and entropy generation abilities of MWCNTs/GNPs hybrid nanofluids in microtubes. *Entropy* **2019**, *21*, 480. [CrossRef]

69. Colangelo, G.; Favale, E.; Milanese, M.; de Risi, A.; Laforgia, D. Cooling of electronic devices: Nanofluids contribution. *Appl. Therm. Eng.* **2017**, *127*, 421–435. [CrossRef]

70. Boruah, M.P.; Randive, P.R.; Pati, S. Effect of non-uniform asymmetric heating on the thermal and entropy generation characteristics for flow of Al_2O_3-water nanofluid in a micro-channel. *Int. J. Numer. Methods Heat Fluid Flow* **2019**, *29*, 981–999. [CrossRef]

71. Shahsavar, A.; Sardari, P.T.; Toghraie, D. Free convection heat transfer and entropy generation analysis of water-Fe_3O_4/CNT hybrid nanofluid in a concentric annulus. *Int. J. Numer. Methods Heat Fluid Flow* **2019**, *29*, 915–934. [CrossRef]

72. Gherasim, I.; Roy, G.; Nguyen, C.T.; Vo-Ngoc, D. Experimental investigation of nanofluids in confined laminar radial flows. *Int. J. Therm. Sci.* **2009**, *48*, 1486–1493. [CrossRef]

73. Brinkman, H.C. The viscosity of concentrated suspensions and solutions. *J. Chem. Phys.* **1952**, *20*, 571. [CrossRef]

74. Chon, C.H.; Kihm, K.D.; Lee, S.P.; Choi, S.U. Empirical correlation finding the role of temperature and particle size for nanofluid (Al_2O_3) thermal conductivity enhancement. *Appl. Phys. Lett.* **2005**, *87*, 153107. [CrossRef]

75. Shah, R.K.; London, A.L. *Laminar Flow Forced Convection in Ducts*; Academic Press: New York, NY, USA, 1978.

76. Duan, Z.P.; Muzychka, Y.S. Slip flow in non-circular microchannels. *Microfluid. Nanofluid.* **2007**, *3*, 473–484. [CrossRef]

77. Duan, Z.P.; Muzychka, Y.S. Slip flow in the hydrodynamic entrance region of circular and noncircular microchannels. *Trans. ASME J. Fluids Eng.* **2010**, *132*, 011201. [CrossRef]

78. Bejan, A. *Entropy Generation through Heat and Fluid Flow*; Wiley: New York, NY, USA, 1982.

79. Duan, Z.P.; Liang, P.; Ma, H.; Ma, N.Y.; He, B.S. Numerical simulation of pressure drop for three-dimensional rectangular microchannels. *Eng. Comput.* **2018**, *35*, 2234–2254. [CrossRef]

80. Jung, J.-Y.; Oh, H.-S.; Kwak, H.-Y. Forced convective heat transfer of nanofluids in microchannels. *Int. J. Heat Mass Transf.* **2009**, *52*, 466–472. [CrossRef]

81. Lee, J.; Mudawar, I. Assessment of the effectiveness of nanofluids for single-phase and two-phase heat transfer in micro-channels. *Int. J. Heat Mass Transf.* **2007**, *50*, 452–463. [CrossRef]

82. Ho, C.J.; Wei, L.C.; Li, Z.W. An experimental investigation of forced convective cooling performance of a microchannel heat sink with Al_2O_3/water nanofluid. *Appl. Therm. Eng.* **2010**, *30*, 96–103. [CrossRef]

83. Hussien, A.A.; Yusop, N.M.; Abdullah, M.Z.; Al-Nimr, M.A.; Khavarian, M. Study on convective heat transfer and pressure drop of MWCNTs/water nanofluid in mini-tube. *J. Therm. Anal. Calorim.* **2019**, *135*, 123–132. [CrossRef]

84. Peyghambarzadeh, S.M.; Hashemabadi, S.H.; Chabi, A.R.; Salimi, M. Performance of water based CuO and Al_2O_3 nanofluids in a Cu–Be alloy heat sink with rectangular microchannels. *Energy Convers. Manag.* **2014**, *86*, 28–38. [CrossRef]

85. Moffat, R.J. Describing uncertainties in experimental results. *Exp. Therm. Fluid Sci.* **1988**, *1*, 3–17. [CrossRef]